Surface Science 664 (2017) 137–146

Contents lists available at ScienceDirect

Surface Science

journal homepage: www.elsevier.com/locate/susc

Role of carrier concentration in swift heavy ion irradiation induced surface modifications

Sushant Gupta [a], V. Ganesan [b], Indra Sulania [c], B. Das [a,*]

[a] Department of Physics, University of Lucknow, Lucknow-226007, India
[b] UGC-DAE Consortium for Scientific Research, Indore-452017, India
[c] Inter University Accelerator Centre (IUAC), New Delhi-110067, India

ARTICLE INFO

Keywords:
Swift heavy ion
Thin films
Point defects
Latent track
Thermal spike model

ABSTRACT

Highly conducting SnO_2 thin films were prepared by chemical spray pyrolysis technique. One set of as-deposited films were annealed in air for 2 h at 850 °C. These as-deposited and annealed SnO_2 thin films were irradiated using gold ions with energy of 120 MeV at different fluences ranging from 1×10^{11} to 3×10^{13} ions/cm^2. Electrical measurement shows that as-deposited SnO_2 films are in conducting state with n = 3.164×10^{20} cm^{-3} and annealed SnO_2 films are in insulating state. The amorphized latent tracks are created only above a certain threshold value of S_e, which directly depends on the free electron concentration (n). The electronic energy loss (S_e) of 120 MeV Au^{9+} ions in SnO_2 is greater than the threshold energy loss (S_{eth}) required for the latent track/molten zone formation in annealed SnO_2 thin film, but is less than S_{eth} required for as-deposited SnO_2 film. Therefore, the latent tracks/molten zones are formed in the annealed SnO_2 film and not in the as-deposited SnO_2 film. Thermal spike model is used for the calculation of threshold energy loss and radius of melted zone. The possible mechanism of the structural changes and surface microstructure evolutions is briefly discussed in the light of ion's energy relaxation processes and target's conductivity. The atomic force microscopy (AFM) study of films shows that the morphologies of irradiated films are linked with carrier concentration of target materials.

1. Introduction

Ion beams can be used in a variety of different ways to synthesize and modify materials on the nanometer scale. By adjusting ion species, ion energy, ion fluence and irradiation geometry it is possible to tailor the ion irradiation conditions for specific needs. In ion beam irradiation process, the kinetic energy of incident ions is transferred to atomic/lattice and electronic systems of solids through elastic collision and electronic excitation/ionization, respectively. The transferred energy to the lattice system induces atomic displacements directly. In the electronic excitation/ionization process, on the other hand, atomic displacements can be caused as a result of indirect energy transfer from irradiating ions [1]. For ions at a higher energy (~ 100 keV/amu), the energy (a few keV/Å) is mainly deposited via electronic excitation and ionization processes [2,3]. In most insulators, when the highly localized energy deposited on target electrons is transferred from the electrons to the target lattice, an extended damage is induced along the ion path: the so-called latent track [3,4]. In metals, however, atomic displacements through the electronic excitation/ionization had been considered to hardly occur because of rapid energy dissipation by a large number of free electrons [4]. In the last two decades, nevertheless, atomic displacements induced by high-density electronic excitation have been found even in pure metallic targets [5,6]. The question of the transformation of the energy deposited by the incident ion during the slowing-down process into energy stored in the target as lattice defects is still to be answered. Two mechanisms have been proposed: (i) The thermal spike (TS) model in which the kinetic energy of target electrons excited by incident ions is transferred to the lattice system through electron-lattice interaction after rapid energy diffusion in the electronic system [7–28]. (ii) The Coulomb explosion (CE) model in which the electrostatic energy of the space charge created just after the ion passage is converted into coherent radial atomic movements leading to a cylindrical shock wave [29]. Both mechanisms are sensitive to the deposited energy density as well as to the rate of energy loss (dE/dx). The TS model of latent track formation is a well established approach that has been successfully applied to insulators, semiconductors, metals, intermetallic compounds and polymers [7–28]. Because of the complexity of all energy relaxation processes involved, this model is also subjected to criticism. However, the TS model seems to be the most elaborated one; furthermore, to our knowledge, currently it is the only model being able to provide at least approximate predictions on latent track formation in numerous conducting and non-conducting targets.

* Corresponding author.
E-mail address: bdas226010@gmail.com (B. Das).

http://dx.doi.org/10.1016/j.susc.2017.06.006
Received 30 January 2017; Received in revised form 31 May 2017; Accepted 9 June 2017
Available online 10 June 2017
0039-6028/

For swift heavy ions (SHI), i.e., ions having velocity comparable to or larger than the orbital electron velocity of the lattice atoms, the energy dissipation in the lattice takes place mainly through ionization and electronic excitation [30–33]. The rapid energy transfer during the electronic excitation can result in a variety of effects in materials including amorphization, defect creation, defect annealing, crystallization, etc. There have been numerous studies on the effects of SHI irradiation in different varieties of targets including insulators, semiconductors and metals, where electronic energy loss ($[dE/dx]_e$) is projected as the major parameter that determines the energy relaxation processes and the resultant effects in materials [30–33]. But if a systematic analysis is done on the effects of SHI irradiation in semiconductors, it can be observed that the effects produced are determined not only by the electronic energy loss ($[dE/dx]_e$) but also by the physical properties of the target materials [34,35]. Several material properties (such as carrier concentration in the present study) that are also influenced by the synthesis conditions seem to decide the ion beam induced effects and are of extreme importance in determining the response of a material to the SHI beam [34]. In this paper we report our studies on the effect of SHI irradiation in SnO_2 polycrystalline thin films differing in their conductivity. There exist few reports in the literature discussing the effect of SHI irradiation on the structural, optical, electrical and sensing properties of SnO_2 thin films grown using different deposition techniques [36–50]. However, no systematic studies have been carried out to verify the role of material properties such as carrier concentration (n) in determining the energy relaxation processes of SHI in SnO_2 thin films.

2. Experimental details

Highly conducting SnO_2 thin films were prepared using chemical spray pyrolysis technique. Dehydrate stannous chloride $SnCl_2.2H_2O$ (Sigma Aldrich purity > 99.99%) was used for making the spray solution for SnO_2 thin films. An amount of 11.281 g of $SnCl_2.2H_2O$ (Sigma Aldrich purity > 99.99%) was dissolved in 5 ml of concentrated hydrochloric acid by heating at 90 °C for 15 min. The addition of HCl rendered the solution transparent, mostly, due to the breakdown of the intermediate polymer molecules. The transparent solution thus obtained and subsequently diluted by methyl alcohol, served as the precursor. The amount of spray solution was made together 50 ml. The spray solution was magnetically stirred for 1 h and finally was filtered by a syringe filter having 0.2 μm pore size before spraying on the substrate. Fused quartz slides (10 mm × 10 mm × 1.1 mm), cleaned with organic solvents, were used as substrates. During deposition, the substrate temperature was maintained at 425 °C. The solution flow rate was maintained at 0.2 ml/min by the nebulizer (droplet size 0.5–10 μm). One set of as-deposited films were annealed in air for 2 h at 850 °C.

To observe the effect of SHI irradiation, these as-deposited and annealed SnO_2 thin films were irradiated with 120 MeV Au ions using a 15 MV pelletron accelerator at Inter University Accelerator Centre (IUAC), New Delhi. Irradiation was done at six different fluences: 1×10^{11}, 3×10^{11}, 1×10^{12}, 3×10^{12}, 1×10^{13} and 3×10^{13} ions/cm^2. The fluence values were estimated by integrating the charges of ions falling on the samples kept inside a cylindrical electron suppressor. The ions were incident perpendicular to the surface of the samples. A high vacuum of 10^{-6} Torr was maintained in the target chamber during the bombardment. Ion beam was raster scanned on the film surface by a magnetic scanner for maintaining a uniform ion flux throughout the film. Beam current was kept constant during experiments and it was around 0.5 particle nanoampere. One sample of each group was left unirradiated in the chamber and was used as the reference sample. We divided our samples into two groups, viz. group A and group B. Group A consists of films which are as-deposited and irradiated (without any post deposition annealing). On the other hand, group B consists of films which underwent post deposition annealing and were further irradiated.

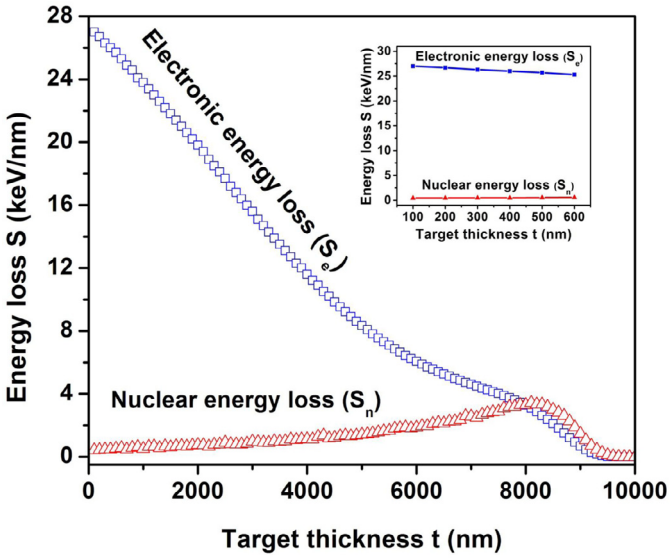

Fig. 1. Variation of nuclear energy loss S_n and electronic energy loss S_e with depth for 120 MeV Au^{9+} ions in SnO_2 matrix as determined by SRIM. Ratio of S_e/S_n is 60. The inset shows the almost constant value of S_e for even 600 nm depth from the surface of the SnO_2 film.

The gross structure and phase purity of all films were examined by X-ray diffraction (XRD) technique using a Bruker AXS, Germany X-ray diffractometer (Model D8 Advanced) operated at 40 kV and 60 mA. In the present study, XRD data of group A and group B thin films were collected in the scanning angle (2θ) range $20° - 60°$ using $Cu - K_\alpha$ radiations (λ = 1.5405 Å). The experimental peak positions were compared with the data from the database Joint Committee on Powder Diffraction Standards (JCPDS) and Miller indices were assigned to these peaks. Atomic force microscopy (AFM) was performed with Multi Mode SPM (Digital Instrument Nanoscope IIIa) in AFM mode to examine the microstructural evolution and root mean square surface roughness of the sample before and after irradiation. Hall measurements were conducted at room temperature to estimate the film resistivity (ρ), donor concentration (n) and carrier mobility (μ) by using the four-point van der Pauw geometry employing Keithley's Hall effect card and switching the main frame system. A specially designed Hall probe on a printed circuit board (PCB) was used to fix the sample of the size 10 mm × 10 mm. Silver paste was employed at the four contacts. The electrical resistivity and the sheet resistance of the films were also determined using the four probe method with spring-loaded and equally spaced pins. The probe was connected to a Keithley voltmeter constant-current source system and direct current and voltage were measured by slightly touching the tips of the probe on the surface of the films. Multiple reading of current and the corresponding voltage were recorded in order to get average values. Thickness of the deposited films was estimated by an Ambios surface profilometer and was approximately 500 nm.

3. Results and discussion

The electronic energy loss (S_e), nuclear energy loss (S_n) and maximum penetrable range (R_p) of the 120 MeV Au ions in SnO_2 are 27.19 keV nm^{-1}, 0.479 keV nm^{-1} and 8490 nm, respectively [51,52]. The variation of S_e and S_n with depth in SnO_2 matrix for 120 MeV Au ions is shown in Fig. 1. Near the surface of the film, S_e exceeds S_n by two orders of magnitude and is almost constant throughout the film thickness, as shown in the inset of Fig. 1. This reveals that the morphological and structural changes in SnO_2 thin film on irradiation by 120 MeV Au^{9+} ions are almost exclusively due to electronic energy losses.

The formation of tracks in materials irradiated in the electronic energy loss regime is the result of complex processes of energy deposition in the electrons, involving several steps: (i) initial energy deposition in the electrons, (ii) energy dissipation among the electrons, leading to a radial expansion of the energy in a cylinder radius between 1 and 10 nm, and (iii) energy transfer to the atoms via the electron-phonon coupling leading to atomic motion and finally to the creation of a cylindrical damage along the ion path.

In the thermal spike (TS) model, the energy deposited in the electrons by the slowing down of the incident ions diffuses within the electron subsystem by electron-electron interactions before being transferred and finally localized in the lattice system via the electron-phonon coupling. The heat diffusion in the electron and in the lattice subsystems versus time t and space r (in cylindrical geometry) is described by the following two coupled nonlinear differential equations [7,8]:

$$C_e(T_e)\frac{\partial T_e}{\partial t} = \frac{1}{r}\frac{\partial}{\partial r}\left[rK_e(T_e)\frac{\partial T_e}{\partial r}\right] - g(T_e - T_a) + A(r,t) \quad (1)$$

$$C_a(T_a)\frac{\partial T_a}{\partial t} = \frac{1}{r}\frac{\partial}{\partial r}\left[rK_a(T_a)\frac{\partial T_a}{\partial r}\right] + g(T_e - T_a) \quad (2)$$

where T, C, and K are the temperatures, the specific heat coefficients, and the thermal conductivities of the electronic (index e) and lattice subsystem (index a), respectively; g is an electron-phonon coupling constant and A(r, t) is the energy density supplied by the incident ion to the electronic system.

At present different ways exist to explore the heat diffusion equations for describing the occurring physical processes and calculating experimentally accessible quantities:

1. The so-called analytical thermal spike (a-TS) model proposed by Szenes [9–15] provides an analytical solution of the differential equation for the atomic system (equation-2) ignoring the way the energy is transferred to the atoms.
2. The ionization diffusion-explosion-amorphization (IDEA) model by Canut and Ramos [16] takes into account the energy diffusion to the electrons prior to its transfer to the atoms by providing an analytical solution of the differential equation for the electronic system (Eq. (1)).
3. In the inelastic thermal spike (i-TS) model [17–27] a complete numerical solution of the system of differential equations [Eqs. (1) and (2)] is given taking into account the coupling between the electronic and atomic subsystems.

In this paper, we have used Szenes' analytical thermal spike model [9–15] to predict the threshold energy loss and radius of melted zone.

To induce melting of the material or to create columnar defects in material a certain threshold value of S_e is required and according to Szenes' [9] "thermal spike model" the value of S_{eth} depends on the material parameters such as density ρ, average specific heat C, melting temperature T_m, irradiation temperature T_{irr}, initial width of the thermal spike a(0), and electron-phonon coupling efficiency g, and can be determined from the following equation:

$$S_{eth} = \frac{\pi\rho C a^2(0)(T_m - T_{irr})}{g} \quad (3)$$

The value of a(0), for semiconductors, depends on their energy band gap E_g, while for insulators it is almost constant. This ion induced thermal spike width a(0) in semiconductors can be best approximated by the expression $a(0) = b + c(E_g)^{\frac{-1}{2}}$ where b and c are constants. Using an E_g value of 3.6 eV for SnO_2, the value of a(0) was determined from the plot of $(E_g)^{\frac{-1}{2}}$ versus a(0) as given in reference-11, and was found to be ~ 6.2 nm. The efficiency with which energy deposited in the electronic subsystem is subsequently transferred to the lattice is governed by the electron-phonon coupling parameter g where typically $g_{insulator} > g_{conductor}$. According to Szenes [9,11], the value of g depends on electron concentration (n). It is found that, for conductive materials (n ≥ 10^{20} cm^{-3}), the value of g is ~ 0.092 [11], while for insulators it is ~ 0.4 [15]. In a later section, we have reported the results of electrical measurements. From these measurements we can say pristine samples of group A (as-deposited SnO_2) are in conducting state with n = 3.164×10^{20} cm^{-3} and pristine samples of group B (annealed SnO_2) are in insulating state. The value of S_{eth} for as-deposited and annealed SnO_2 films was calculated from Eq. (3) by substituting the values of material density (ρ = 6.99 g/cm^3), average specific heat (C = 0.3490 J/gK), melting temperature (T_m = 1898 K) [53,54], irradiation temperature (T_{irr} = 300 K) for SnO_2. For the as-deposited SnO_2 films the threshold value of track formation or amorphization S_{eth} (estimated by using a(0) = 6.2 nm and g = 0.092 [11]) is 31.92 keV nm^{-1}. In this case, the S_e value is less than the threshold value required to induce amorphization/melting of material and we expect that only point defects or clusters of point defects will be produced in as-deposited SnO_2 thin films. For annealed SnO_2 films the value of S_{eth} (calculated by using a(0) = 4.5 nm and g = 0.4 [15]) is 3.868 keV nm^{-1}, which is much smaller than the available S_e of 27.19 keV nm^{-1} induced by 120 MeV Au^{9+} ions. Therefore, latent track formation/amorphization/melting is only possible in the annealed films (samples of group B) but not in the as-deposited films (samples of group A). The value of threshold electronic energy loss S_{eth} in as-deposited and annealed SnO_2 films along with values of S_e, S_n and R are listed in the Table 1. For permanent damage, the maximum temperature reached at the some local region needs to be significantly higher than the melting temperature (1898 K for SnO_2). The structure of grains is changed (spherical to ribbon/rod like) only when melting is observed and the nature/size of the new structure corresponded closely to the maximum molten region.

Table 1
The values of nuclear energy loss (S_n), electronic energy loss (S_e), and range (R_p) for 120 MeV Au^{9+} ions in a SnO_2 thin film estimated by SRIM [51,52]. The threshold value of electronic energy loss (S_{eth}) and possibility of latent track formation are also mentioned.

Parameters	SnO_2 (as-deposited)	SnO_2 (annealed)
Nuclear energy loss	0.479 keV nm^{-1}	0.479 keV nm^{-1}
Electronic energy loss	27.19 keV nm^{-1}	27.19 keV nm^{-1}
Threshold energy loss	31.92 keV nm^{-1}	3.868 keV nm^{-1}
Range	8.49 μm	8.49 μm
Track formation	Not possible	Possible

The basic assumption of Szenes' thermal-spike model [9] is that around the path of the swift heavy ion a high-temperature region is formed in the material. It is assumed that when the temperature exceeds the melting point of the material a melt is formed. Due to its small diameter, the cooling rate of the melt may reach 10^{13} - 10^{14} K/s that results in an amorphous structure when the melt solidifies [9,19]. In this model [9], time zero is chosen when the lattice temperature on the track axis attains its maximum/peak value (T_p) and time t is measured from that moment (see Fig. 2). Let us denote by T_{irr}, T_m, T(r,t) the target temperature during irradiation, the melting point, and the temperature at a distance r from the ion path, respectively. If $\Delta T(r, t)$ is the local temperature increase in the thermal spike then $T(r,t) = T_{irr} + \Delta T(r, t)$. This $\Delta T(r, t)$ can be described by a radial Gaussian distribution:-

$$\Delta T(r,t) = \frac{Q}{\pi a^2(t)} e^{\frac{-r^2}{a^2(t)}} \quad (4)$$

where Q = (gS_e - $L\rho\pi R^2$)/(ρC) is determined by (partial) energy conservation and $a^2(t) = a^2(0) + 4kt/(\rho C)$ denotes the width of the temperature profile at later times. The quantities R = R(t) is the radius of the melted zone, ρ, C and L are the density, the mean specific heat, and the latent heat of melting, respectively. The parameter g determines the fraction of electronic excitation energy which is converted to heat at time zero. Here, the approximation $gS_e \gg L\rho\pi R^2$ will be used. This is usually valid for materials in which $S_e > S_{eth}$ is observed. Interestingly,

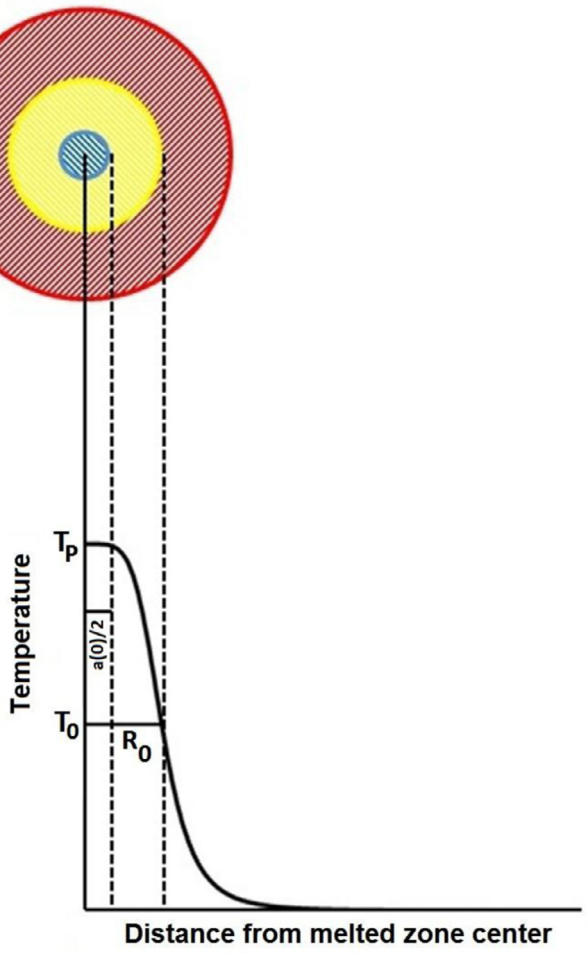

Fig. 2. Formation of a melted zone around the swift heavy ion path in the annealed SnO_2 film. a(0) and R_0 are the width of the thermal spike and latent track/melted zone radius, respectively. The central blue (dark) color region shows the width of the thermal spike, a(0), and its adjacent yellow (light) color region on both sides shows the thermal-spike-induced latent track/melted zone in the annealed SnO_2 film. T_P and $T_0 = T_m - T_{irr}$ are the peak temperature and thermal spike temperature required for melting the SnO_2 film, respectively. (For interpretation of the references to color in this figure legend, the reader is referred to the web version of the article). (For interpretation of the references to color in this figure legend, the reader is referred to the web version of this article.)

Szenes [9] found a correlation between the threshold electronic energy loss for track formation , S_{eth}, and the thermal energy required to reach the melting temperature. The target material melts in the region where its temperature $(\Delta T + T_{irr})$ exceeds the melting point T_m of material. Therefore, to reach the melting point the temperature in the thermal spike should be increased by $T_0 = T_m - T_{irr}$. The maximum value R = R_0 can be obtained from the condition dr/dt = 0 at $\Delta T = T_0$. If the temperature at r = a(t) is denoted by T_a then R = R_0 when $T_a = T_0$. The width of the temperature distribution a(t) increases and T_a decreases with time in the cooling spike. If initially $T_0 > T_a$, at t = 0 [R(0) < a(0)], then $T_0 = T_a$ never fulfills and the melted zone will have its maximum diameter at t = 0. If $T_0 < T_a$ at t = 0 [R(0) > a(0)] then the melted zone expands up to t = t' when $T_a = T_0$, [R_0 = R(t') = a(t')] and further it shrinks for t > t' (see Fig. 2). Thus, the two simple equations for radius of melted zone (track radius) was obtained by Szenes [9,13] using the condition of maxima in Eq. (4).

$$R_0^2 = a^2(0)\ln\left[\frac{S_e}{S_{eth}}\right], \quad 1 \le \frac{S_e}{S_{eth}} \le 2.7 \tag{5}$$

$$R_0^2 = \left[\frac{a^2(0)}{2.7}\right]\frac{S_e}{S_{eth}}, \quad \frac{S_e}{S_{eth}} > 2.7 \tag{6}$$

According to Eq. (5) there is a threshold electronic energy loss S_{eth} below which no melting/amorphization is predicted and at this point $T_p = T_0$. Expression 5 describes a logarithmic variation of the melted zone cross section A = πR_0^2 in the $1 < \frac{S_e}{S_{eth}} < 2.7$ range. Expression 6 is an equation of a straight line for $S_e/S_{eth} > 2.7$ going through the origin. There is a smooth transition between the linear and logarithmic regimes. At $S_e = 2.7S_{eth}$, both expressions provide the same value for track radius.

The value of S_e/S_{eth} ratio for annealed SnO_2 samples is ~ 7.0. The approximate value of radius of melted zone (R_0) in annealed SnO_2 samples has been calculated from Eq. (6) as 7.26 nm. Since the estimated melted zone diameter is ~ 14.52 nm, the 1 cm^2 sample will be fully covered with melted zones/ion tracks at a fluence of about 6 × 10^{11} ions/cm^2, corresponding to $1/\pi R_0^2$. Thus, beyond this critical fluence (> 6 × 10^{11} ions/cm^2) there will be a considerable overlapping of melted zones.

To understand the structural modifications induced by SHI irradiations, we have performed X-ray diffraction measurements. Fig. 3(a) shows the XRD patterns for group A samples. The group A samples turn out to be polycrystalline in nature with (110), (101), (200) and (211) planes of tetragonal rutile tin oxide. It is clear from XRD patterns of group A samples that there is no reduction in crystallinity after irradiation. The amorphization is induced in crystalline lattice only above a certain threshold value of S_e, which directly depends on the free electron concentration (n). In a later section, we have reported the results of Hall measurements. From these measurements we can say as-deposited SnO_2 samples are in conducting state with n ≥ 10^{20} cm^{-3}. These conduction electrons rapidly spread the energy of incident-ion throughout the material. Therefore, as-deposited samples require high beam energy to induce amorphization in crystalline lattice. But in the present case the value of S_e (~ 27.19 keV nm^{-1}) is less than the threshold value (S_{eth} ~ 31.92 keV nm^{-1}) required to induce amorphization in as-deposited samples. Consequently, we except that only point defects or cluster of point defects will be produced after irradiation. Fig. 3(b) presents the XRD patterns of group B films. The pristine XRD pattern of group B reveals four prominent peaks ((110), (101), (200) and (211)) corresponding to tetragonal rutile structure of SnO_2. The growth of tin oxide nano-crystals and thus improvement in crystallinity after annealing is a common phenomenon [55]. From Fig. 3(b), it is observed that intensity of diffraction peaks decreases for the films irradiated with the fluence of 1 × 10^{11} and 3 × 10^{11} ions/cm^2. The decrease of peak intensity is due to reduction in crystallinity of the annealed SnO_2 film. Further, with increase in ion fluence, the diffraction peaks completely disappear at the fluence of 1 × 10^{12} ions/cm^2. The sample in this case is amorphized as a result of cascade quenching with SHI irradiation. The structural modification induced by SHI irradiation can be explained by total energy deposited in electronic excitations or ionizations in the films by energetic ion. The imparted energy of the incoming ions in annealed films at higher fluence may result in overlapping of tracks to cause lattice disordering inside grains. The value of threshold electronic energy loss S_{eth} for annealed samples is very less than that of as-deposited samples. Therefore, 120 MeV Au^{9+} ions are sufficient to induce amorphization in crystalline lattice of annealed samples.

The electrical properties of the films were estimated by resistivity and Hall effect measurements made at room temperature. The room temperature results are presented for all measured films in Table 2. The as-deposited SnO_2 films (pristine samples of group A) show the best combination of electrical properties as follows: resistivity (ρ) of 1.75 × 10^{-3} Ω cm, carrier concentration (n) of 3.164 × 10^{20} cm^{-3}, and mobility (μ) of 11.291 cm^2 V^{-1} s^{-1}. In contrast, the resistivity of the thermally annealed films (pristine samples of group B) shows an insulating behavior. It has long been thought that native defects such as oxygen vacancy V_O and tin interstitial Sn_i are responsible for the observed n-type conductivity. First principle calculations have provided evidence that usual suspects such as oxygen vacancy V_O and tin interstitial Sn_i are actually not responsible for n-type conductivity in majority of the

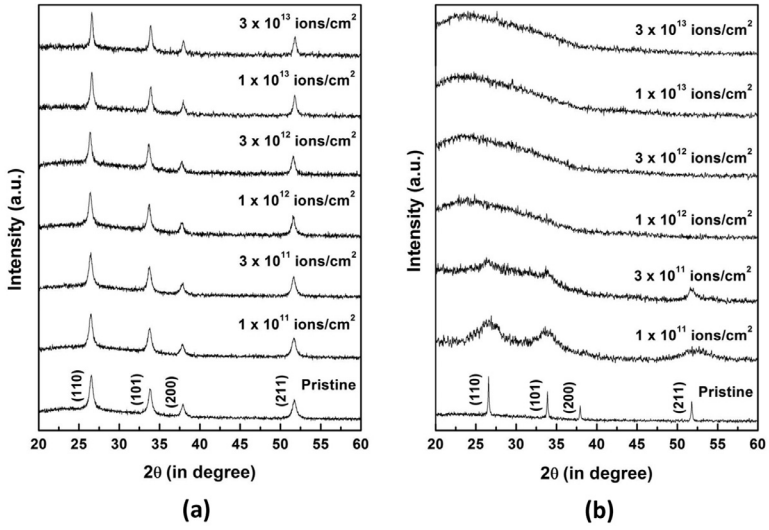

Fig. 3. X-ray diffraction patterns of (a) group A and (b) group B thin films.

cases [56–58]. These calculations indicate that the oxygen vacancies are a deep donor, whereas tin interstitials are too mobile to be stable at room temperature [57]. Recent first principle calculations have drawn attention on the role of donor impurities in unintentional n-type conductivity [56–62]. Hydrogen is indeed a especially ambidextrous impurity in this respect, since it is extremely difficult to detect experimentally [56–58]. By means of density functional calculations it has been shown that hydrogen can substitute on an oxygen site and has a low formation energy and act as a shallow donor [56–58]. Hydrogen is by no means the only possible shallow donor impurity in tin oxide, but it is a very likely candidate for an impurity that can be unintentionally incorporated and can explain observed unintentional n-type conductivity [58]. Several groups have reported on the incorporation of hydrogen in tin oxide and many have claimed that hydrogen substitutes for oxygen [56,57,63–77]. In the thermally annealed film, the transformation towards stoichiometry leads to an increase in the resistivity as expected for a metal-oxide semiconductor. Thermal annealing of as-deposited SnO_2 films has been carried out beyond the migration temperature of H_O^+ defects (~ 900 K) [56,57,76,77] to confirm the role of H_O^+ defects on the film resistivity.

Measurement of resistivity, carrier density, and mobility as a function of ion fluence (1×10^{11} to 3×10^{13} ions/cm^2) promulgates that increasing fluence results in degradation in electrical properties of as-deposited SnO_2 (see Table 2). The electrical resistivity of as-deposited SnO_2 thin films increases from 1.75×10^{-3} to 152 Ω cm, the carrier density and mobility decrease from 3.164×10^{20} to 8.692×10^{15} cm^{-3} and from 11.291 to 4.728 cm^2 V^{-1} s^{-1} with increasing ion fluence from 1×10^{11} to 3×10^{12} ions/cm^2. In addition, electrical measurements above 3×10^{12} ions/cm^2 show that the sheet resistance of irradiated films is of the order of 10 MΩ/ □. The swift heavy ion irradiation is a very effective technique to create point defects in the lattice of conducting target material (when $S_e < S_{eth}$). Both donor (Sn_O^{4+}) and acceptor (V_{Sn}^{4-}, O_i^{2-}, O_{Sn}^{2-}) type of native defects can be created with the help of ion beam. The concentration of native defects depends on their formation energies. A low formation energy implies a high concentration of the defect and a high formation energy means defects are unlikely to form. SHI irradiation can also anneal-out the pre-existing defects (H_O^+) of as-deposited samples. Self-annealing is a process through which pre-existing defects of target are annealed out. Self-annealing of pre-existing defects (H_O^+) depends upon the ion fluence of irradiation. Almost all pre-existing defects (H_O^+) may anneal-out at high fluence. In this process, the energy transfer through ion-electron interaction makes the target abnormally excited. The electrical properties of irradiated films could be influenced by both self-annealing of pre-existing defects and formation of new point defects.

The temperature dependence of electrical resistivity in the range 30–200 °C indicates that as-deposited SnO_2 films (pristine samples of group A) are degenerate semiconductors. The film degeneracy was further confirmed by evaluating degeneracy temperature T_D of the electron gas by the expression [78,79]:

$$T_D \simeq \left(\frac{\hbar^2}{2m^* k_B}\right)(3\pi^2 n)^{\frac{2}{3}} = E_F/k_B, \tag{7}$$

where m^* is the reduce effective mass and n is the electron concentration. The degeneracy temperature of all investigated samples is clearly displayed in Table 2. It can be seen that T_D of as-deposited SnO_2 (pristine) films are well above room temperature, at around 6000 K. Here, we have tried to identify the main scattering mechanisms that influence the mobility of as-deposited SnO_2 films. There are many scattering mechanisms such as grain-boundary scattering, domain scattering, surface scattering, interface scattering, phonon scattering (lattice vibration), neutral, and ionized impurity scattering which may influence the mobility of the films [80,81]. The interaction between the scattering centres and the carriers determines the actual value of the mobility of the carriers in the samples. In the interpretation of the mobility obtained for as-deposited SnO_2 films, one has to deal with the problem of mixed scattering of carriers. To solve this problem, one has to identify the main scattering mechanism and then determine their contributions. The SnO_2 films prepared here are polycrystalline. They are composed of grains joined together by grain boundaries, which are transitional regions between different orientations of neighboring grains. These boundaries between grains play a significant role in the scattering of charge carriers in polycrystalline thin films. The grain boundary scattering has an effect on the total mobility only if the grain size is approximately of the same order as the mean free path of the charge carriers ($D \sim \lambda$). The mean free path for the degenerate samples can be calculated from known mobility (μ) and carrier concentration (n) using the following expression [79,81]:

$$\lambda = (3\pi^2)^{\frac{1}{3}}\left(\frac{\hbar\mu}{e}\right)n^{\frac{1}{3}}, \tag{8}$$

The mean free path value calculated for the as-deposited SnO_2 film is 1.569 nm which is considerable shorter than grain size (D ~ 50 nm) estimated using AFM. Moreover, the effect of crystallite interfaces is weaker in semiconductors, with n ≥ 10^{20} cm^{-3}, observed here, as a

Table 2
Electrical parameters for all the samples.

Samples	Group A			Degeneracy temperature T_D (K)	Carrier mobility μ ($cm^2V^{-1}s^{-1}$)		Group B
	Sheet resistance R_s	Resistivity ρ (Ω cm)	Carrier concentration n (cm^{-3})		Observed	Calculated	Sheet resistance R_s
Pristine	35 Ω/□	1.75×10^{-3}	3.164×10^{20}	6360	11.291	9.747	> 10 MΩ/□
1×10^{11} ions/cm^2	1.07 kΩ/□	5.47×10^{-2}	1.357×10^{19}	779	8.423	–	> 10 MΩ/□
3×10^{11} ions/cm^2	9.49 kΩ/□	0.498	2.381×10^{18}	244	5.274	–	> 10 MΩ/□
1×10^{12} ions/cm^2	0.483 MΩ/□	24.4	5.157×10^{16}	19	4.965	–	> 10 MΩ/□
3×10^{12} ions/cm^2	3.17 MΩ/□	152	8.692×10^{15}	6	4.728	–	> 10 MΩ/□
1×10^{13} ions/cm^2	> 10 MΩ/□	–	–	–	–	–	> 10 MΩ/□
3×10^{13} ions/cm^2	> 10 MΩ/□	–	–	–	–	–	> 10 MΩ/□

consequence of the narrower depletion layer width at the interface between two grains [82]. Based on above discussion it is concluded that grain boundary scattering is not a dominant mechanism.

The mobility of the free carrier is not affected by surface scattering unless the mean free path is comparable to the film thickness [83]. Mean free path value calculated for the as-deposited SnO_2 film is 1.569 nm, which is much smaller than the film thickness (t~ 500 nm). Hence, surface scattering can be ruled out as the primary mechanism. Scattering by acoustical phonons [84] apparently plays a subordinate role in the as-deposited SnO_2 films because no remarkable temperature dependence have been observed between 30 and 200 °C. Moreover, neutral impurity scattering can be neglected because the neutral defect concentration is negligible in the as-deposited SnO_2 films [79,81]. Electron-electron scattering, as suggested to be important in Ref. [81], can also be neglected as it does not change the total electron momentum and thus not the mobility. In high crystalline SnO_2 films, scattering by dislocations and precipitation is expected to be of little importance [85].

Another scattering mechanism popular in unintentionally doped semiconductors is the ionized impurity scattering. According to the Brooks-Herring formula [86], the relaxation time for coupling to ionized impurities is in the degenerate case, given by

$$\tau_i = \frac{(2m^*)^{\frac{1}{2}}(\epsilon_o\epsilon_r)^2(E_F)^{\frac{3}{2}}}{\pi e^4 N_i f(x)}, \tag{9}$$

with N_i the carrier concentration of ionized impurities and f(x) given by

$$f(x) = ln(1+x) - \frac{x}{1+x}, \tag{10}$$

with

$$x = \frac{8m^* E_F R_S^2}{\hbar^2}, \tag{11}$$

The screening radius R_S is given by

$$R_S = \left(\frac{\hbar}{2e}\right)\left(\frac{\epsilon_o\epsilon_r}{m^*}\right)^{\frac{1}{2}}\left(\frac{\pi}{3N_i}\right)^{\frac{1}{6}}, \tag{12}$$

where ϵ_r is the relative dielectric permittivity and m^* is the effective mass of the carriers. The mobility (μ) is defined as

$$\mu = \frac{e\tau}{m^*}, \tag{13}$$

Substitution of the τ_i expression [Eq. (9)] in Eq. (13) yields the expression for mobility due to ionized impurities as

$$\mu_i = \frac{(\frac{2}{m^*})^{\frac{1}{2}}(\epsilon_o\epsilon_r)^2(E_F)^{\frac{3}{2}}}{\pi e^3 N_i f(x)}, \tag{14}$$

Since all the H_O^+ defects present in the as-deposited SnO_2 films will be fully ionized at room temperature, impurity ion concentration will be equal to the free carrier concentration. Thus taking N_i = n, m^* = 0.31 m, ϵ_r = 13.5 [53] and using Eq. (7) in Eq. (14) we get simplified form as

$$\mu_i = \frac{2.4232 \times 10^{-4}}{f(x)}, \tag{15}$$

with

$$x = 1.7942 \times 10^{-9} n^{\frac{1}{3}}, \tag{16}$$

The calculated mobility and measured mobility values for as-deposited SnO_2 thin films are 9.747 and 11.291 cm^2 V^{-1} s^{-1} respectively, both are comparable to each other. This clearly indicates that the main scattering mechanism reducing the intra-grain mobility of the electrons in as-deposited SnO_2 films is the ionized impurity scattering. Ionized impurity scattering with singly ionized H_O^+ donors best describes the mobility of as-deposited SnO_2 samples. This finding supports our assumption that H_O^+ defect is source of conductivity in as-deposited SnO_2 sample. The mobility of electrons in non-degenerate semiconductor increases with temperature and is independent of the electron concentration,

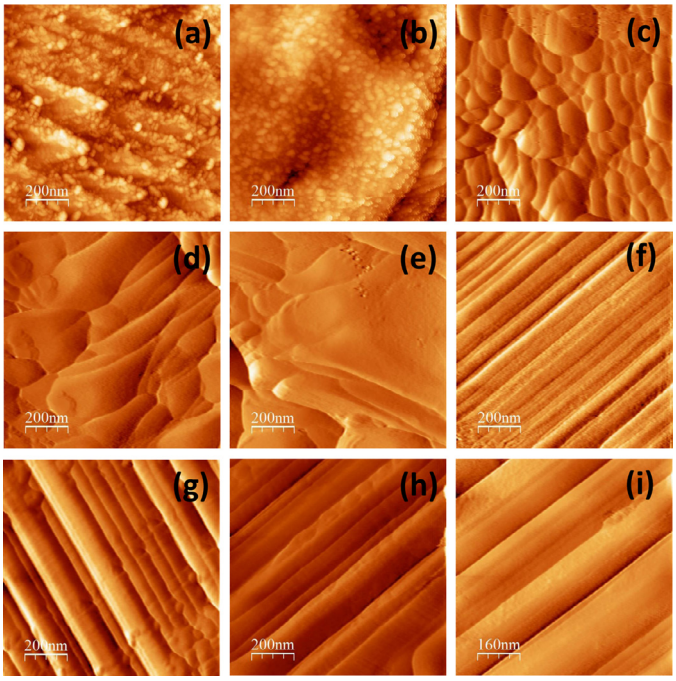

Fig. 4. Atomic force microscopy images of SnO_2 surfaces: (a) group A - pristine sample, (b) group A - 3×10^{13} ions/cm^2 irradiated sample, (c) group B - pristine sample, (d) group B - 1×10^{11} ions/cm^2 irradiated sample, (e) group B - 3×10^{11} ions/cm^2 irradiated sample, (f) group B - 1×10^{12} ions/cm^2 irradiated sample, (g) group B - 3×10^{12} ions/cm^2 irradiated sample, (h) group B - 1×10^{13} ions/cm^2 irradiated sample, (i) group B - 3×10^{13} ions/cm^2 irradiated sample.

whereas the mobility in a highly degenerate semiconductor is nearly independent of temperature and increases with electron concentration [87,88].

The surface morphology of group A and group B samples were investigated by atomic force microscopy (AFM) using a NanoScope IIIa from Digital Instruments operating in tapping mode. Fig. 4 shows the AFM micrographs of group A and group B samples. Fig. 4(a) shows the morphology of the as-deposited SnO_2 film (pristine sample of group A) which has nanostructures with broader size distribution in the range from 15 to 50 nm. The root mean square (rms) roughness is 5 nm. When this as-deposited SnO_2 film is irradiated with 3×10^{13} ions/cm^2 (Fig. 4(b)), there is a significant increment in rms roughness (23 nm) and crystallite size. The dimension of nanostructures becomes 30 to 60 nm. Fig. 4(c) shows the surface morphology of an annealed SnO_2 film (pristine sample of group B). After annealing, the nanostructures become almost spherical in shape with size in the range of 50 to 150 nm and rms roughness of 15 nm. The increment in grain size is caused due to the thermal heating induced growth in crystallinity. These grains are aligned in a particular direction leading to increment in rms roughness.

It is clear from the Fig. 4(c) that annealed SnO_2 films show granular nanostructure with distinct grain boundary. Fig. 4(d)–(i) shows surface morphologies of the annealed samples irradiated with 1×10^{11}, 3×10^{11}, 1×10^{12}, 3×10^{12}, 1×10^{13} and 3×10^{13} ions/cm^2, respectively. The irradiated samples of group B show that nanostructures get started to alteration at the lower irradiation fluence of 1×10^{11} ions/cm^2. The grains are still distinct and not cobbled together at lower irradiation fluence. Remarkable changes can be seen in 3×10^{11} ions/cm^2 fluence irradiated film. The nanostructures get entirely smashed via eliminating boundaries and the new aggregated grains of unusual morphology are appeared on the sample surface. This arrangement of structures, under SHI irradiation, is expected to be governed by the confinement of a high density of energy of bombarding ions in the volume of individual grains and grain diffusion process. Fig. 4(i) shows the surface of the group B film irradiated with 3×10^{13} ions/cm^2 fluence. Morphology of this film is very much different from that shown in Fig. 4(b). At this condition nanoribbon/nanorod like structures with size in the range of 200–300 nm and rms roughness of 15 nm are grown in lateral direction on the surface. The details of the morphological studies are summarized in Table 3. Morphology of irradiated film depends on the conductivity of target material. If the target material is a conductor (pristine sample of group A: $n \geq 10^{20}$ cm^{-3}) then conduction electrons rapidly spread the energy of incident ion throughout the material and we find similar pristine/target sample like morphology with some dimensional change after irradiation (see Fig. 4(a) and (b)). But if target material is an insulator (such as pristine sample of group B) then projectile ions can not spread their energy throughout the target material and therefore they create high energy region in the close vicinity of their paths. This cylindrical region around the path of the ion may become fluid if maximum temperature reached at the centre is higher than the melting temperature of the material. The structure of grains is changed (spherical to ribbon/rod like) only when melting is observed and the nature/size of the new structure corresponded closely to the maximum molten region. The approximate value of molten zone radius on the annealed SnO_2 film surface is ~ 7.26 nm. By considering 14.52 nm as the diameter of the molten zone on the annealed film surface, the critical fluence to cover the total surface with molten zones is found to be about 6×10^{11} ions/cm^2. Thus, beyond this critical fluence there will be a considerable overlapping of molten zones (See Fig. 5). The nanoribbon/nanorod like morphology was first observed at 1×10^{12} ions/cm^2, which is higher than the value 6×10^{11} ions/cm^2 of ion fluence. This shows that the nanoribbon/nanorod like structures are not created by single-ion impact but rather they are the result of overlapping of molten zones. The typical amorphous nanoribbon/nanorod like structures could arise on the surface of the high fluence ($> 6 \times 10^{11}$ ions/cm^2) irradiated films due to rapid resolidification of the molten layer. According to the principles of solidification [89], the morphology of solidified material is controlled by the temperature gradient (G) in the liquid near the advancing interface and by the growth rate (R). Melt recoil pressure, surface tension, diffusion and evaporation dynamics could also affect the resolidification process of molten layer and consequently the structure of grains.

Table 3
Morphological studies for all the samples.

Samples	Group A			Group B		
	Particle shape	Particle size	Rms roughness	Particle shape	Particle size	Rms roughness
Pristine	Spherical	15–50 nm	5 nm	Spherical	50–150 nm	15 nm
1×10^{11} ions/cm^2	Spherical	15–50 nm	10 nm	Irregular	–	21 nm
3×10^{11} ions/cm^2	Spherical	20–50 nm	12 nm	Irregular	–	13 nm
1×10^{12} ions/cm^2	Spherical	20–55 nm	15 nm	Ribbon/Rod-like	50–150 nm thick	8 nm
3×10^{12} ions/cm^2	Spherical	20–55 nm	13 nm	Ribbon/Rod-like	50–150 nm thick	16 nm
1×10^{13} ions/cm^2	Spherical	30–60 nm	25 nm	Ribbon/Rod-like	50–200 nm thick	15 nm
3×10^{13} ions/cm^2	Spherical	30–60 nm	23 nm	Ribbon/Rod-like	200–300 nm thick	15 nm

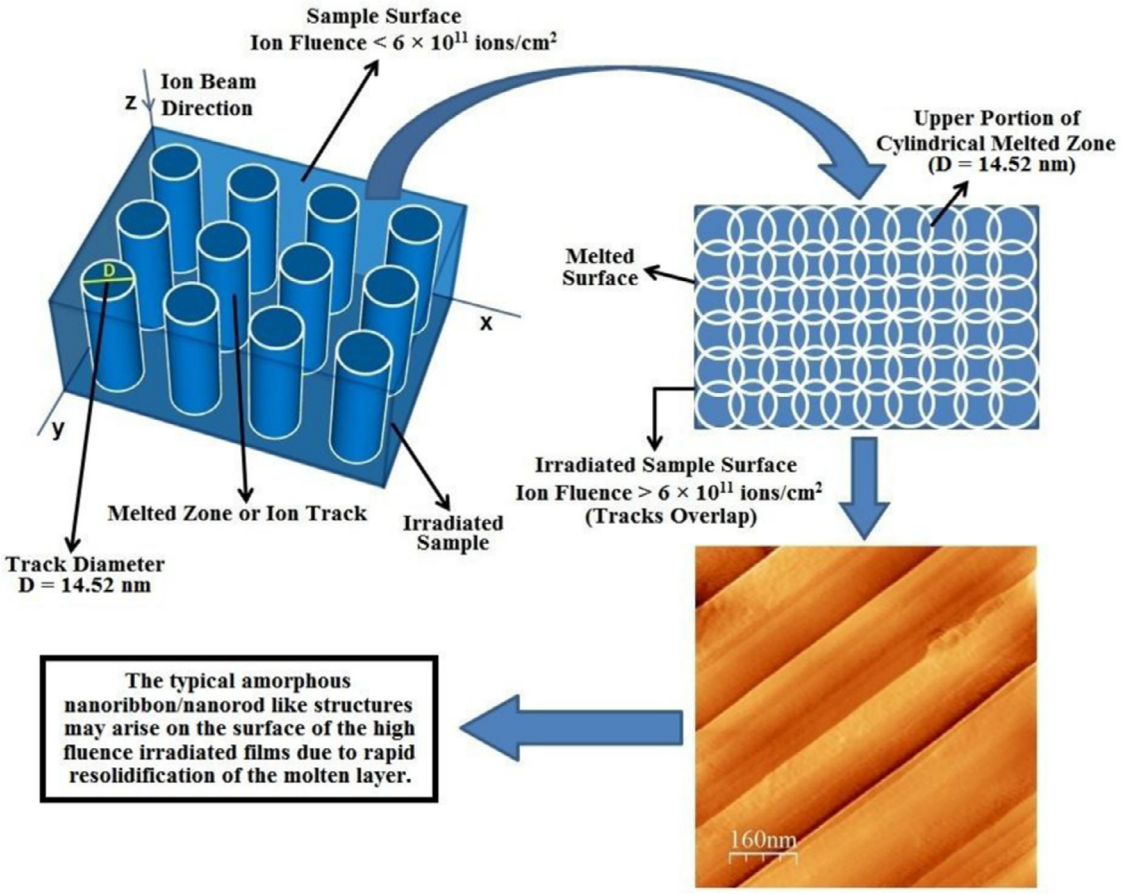

Fig. 5. Schematic illustration of the formation mechanism of nanoribbon/nanorod like structures.

4. Conclusions

Highly conducting SnO_2 thin films were successfully deposited by spray pyrolysis technique on quartz substrates at 425 °C. One set of as-deposited films were annealed in the air by increasing the substrate temperature to 850 °C for 2 h. These as-deposited and annealed films were irradiated with 120 MeV Au^{9+} ions at six fluence values of 1×10^{11}, 3×10^{11}, 1×10^{12}, 3×10^{12}, 1×10^{13} and 3×10^{13} ions/cm^2 using 15 MV Pelletron tandem accelerator. The analysis of X-ray diffraction patterns reveals that the as-deposited and annealed tin oxide thin films are pure crystalline with tetragonal rutile phase of tin oxide which belongs to the space group $P4_2/mnm$ (number 136). Electrical measurement shows that as-deposited SnO_2 films are in conducting state with $n = 3.164 \times 10^{20}$ cm^{-3} and annealed SnO_2 films are in insulating state. The results of electrical measurements suggest that H_O^+ defects in as-deposited SnO_2 thin films are responsible for the conductivity. Through electrical investigation it has also been found that the main scattering mechanism reducing the intra-grain mobility of the electrons in as-deposited SnO_2 films is the ionized impurity scattering. Ionized impurity scattering with singly ionized H_O^+ donor best describes the mobility of as-deposited SnO_2 samples. The amorphized latent tracks are created only above a certain threshold value of S_e, which directly depends on the free electron concentration (n). The electronic energy loss (S_e) of 120 MeV Au^{9+} ions in SnO_2 is greater than the threshold energy loss (S_{eth}) required for the latent track formation in annealed SnO_2 thin film, but is less than S_{eth} required for as-deposited SnO_2 film. Therefore, the latent tracks are formed in the annealed SnO_2 film and not in the as-deposited SnO_2 film. Thermal spike model is used for the calculation of threshold energy loss and radius of melted zone. The possible mechanism of the structural changes and surface microstructure evolutions is briefly discussed in the light of ion's energy relaxation processes and target's conductivity. The atomic force microscopy (AFM) study of films reveals that the morphologies of irradiated films are linked with carrier concentration of target materials.

Acknowledgments

One of the authors (Sushant Gupta) is thankful to Inter University Accelerator Centre (IUAC), New Delhi for awarding Research Fellowship through the UFUP Project scheme (Project No. UFR-49311). The authors gratefully acknowledge to D. Kanjilal, F. Singh, A. Tripathi, K. Asokan, P. K. Kulriya, IUAC, New Delhi and M. Gupta, M. Gangrade, UGC-DAE Consortium for Scientific Research, Indore for providing the characterization facilities. We thank Pelletron group, IUAC, New Delhi for expert assistance in the operation of the tandem accelerator. Also authors sincerely thank reviewers for valuable suggestions to improve the quality and standard of the manuscript.

References

[1] G. Dearnaley, Ion bombardment and implantation, Rep. Prog. Phys. 32 (1969) 405–491.
[2] N. Itoh, A.M. Stoneham, Materials Modification by Electronic Excitation, Cambridge University Press, Cambridge, 2001.
[3] N. Itoh, D.M. Duffy, S. Khakshouri, A.M. Stoneham, Making tracks: electronic excitation roles in forming swift heavy ion tracks, J. Phys.: Condens. Matter 21 (2009) 1–14. 474205.
[4] D. Kanjilal, Swift heavy ion-induced modification and track formation in materials, Curr. Sci. 80 (2001) 1560–1566.
[5] A. Iwase, T. Iwata, Effect of electron excitation on radiation damage in fce metals, Nucl. Instrum. Methods Phys. Res. B 90 (1994) 322–329.
[6] A. Dunlop, D. Lesueur, P. Legrand, H. Dammak, J. Dural, Effects induced by high electronic excitations in pure metals: a detailed study in iron, Nucl. Instrum. Methods Phys. Res. B 90 (1994) 330–338.

[7] I.M. Lifshitz, M.I. Kaganov, L.V. Tanararov, On the theory of radiation-induced changes in metals, J. Nucl. Energy A 12 (1960) 69–78.
[8] C. Dufour, M. Toulemonde, et al., Models for the description of track formation, in: W. Wesch (Ed.), Ion Beam Modification of Solids, Springer Series in Surface Sciences, 2016.
[9] G. Szenes, General features of latent track formation in magnetic insulators irradiated with swift heavy ions, Phys. Rev. B 51 (1995a) 8026–8029.
[10] G. Szenes, Ion-velocity-dependent track formation in yttrium iron garnet: a thermal-spike analysis, Phys. Rev. B 52 (1995b) 6154–6157.
[11] G. Szenes, Z.E. Horvath, B. Pecz, F. Paszti, L. Toth, Tracks induced by swift heavy ions in semiconductors, Phys. Rev. B 65 (2002) 1–11. 045206.
[12] G. Szenes, Information provided by a thermal spike analysis on the microscopic processes of track formation, Nucl. Instrum. Methods Phys. Res. B 191 (2002) 54–58.
[13] G. Szenes, A possible mechanism of formation of radiation defects in amorphous metals, Mater. Sci. Forum 97–99 (1992) 647–652.
[14] G. Szenes, K. Havancsák, V. Skuratov, P. Hanák, L. Zsoldos, T. Ungár, Application of the thermal spike model to latent tracks induced in polymers, Nucl. Instrum. Methods Phys. Res. B 166–167 (2000a) 933–937.
[15] G. Szenes, F. Pászti, Á, Péter, A.I. Popov, Tracks induced in TeO_2 by heavy ions at low velocities, Nucl. Instrum. Methods Phys. Res. B 166/167 (2000b) 949–953.
[16] B. Canut, S.M.M. Ramos, The concept of effective electronic stopping power for modelling the damage cross-section in refractory oxides irradiated by Gev ions or Mev clusters, Radiat. Eff. Defects Solids 145 (1998) 1–27.
[17] M. Toulemonde, C. Dufour, A. Meftah, E. Paumier, Transient thermal processes in heavy ion irradiation of crystalline inorganic insulators, Nucl. Instrum. Methods Phy. Res. Sect. B 166–167 (2000) 903–912.
[18] M. Toulemonde, C. Dufour, E. Paumier, Transient thermal process after a high-energy heavy-ion irradiation of amorphous metals and semiconductors, Phys. Rev. B 46 (1992) 14362–14369.
[19] M. Toulemonde, J.M. Costantini, C. Dufour, A. Meftah, E. Paumier, F. Studer, Track creation in SiO_2 and $BaFe_{12}O_{19}$ by swift heavy ions: a thermal spike description, Nucl. Instrum. Methods Phys. Res. B 116 (1996) 37–42.
[20] C. Trautmann, M. Toulemonde, C. Dufour, E. Paumier, Effect of the radial energy distribution on the ion track etching in amorphous metallic $Fe_{81}B_{13.5}Si_{3.5}C_2$, Nucl. Instrum. Methods Phys. Res. Sect. B 108 (1996) 94–98.
[21] A. Meftah, F. Brisard, J.M. Costantini, E. Dooryhee, M. Hage-Ali, M. Hervieu, J.P. Stoquert, F. Studer, M. Toulemonde, Track formation in SiO_2 quartz and the thermal spike mechanism, Phys. Rev. B 49 (1994) 12457–12463.
[22] A. Meftah, M. Djebara, N. Khalfaoui, M. Toulemonde, Sputtering of vitreous SiO_2 and $Y_3Fe_5O_{12}$ in the electronic stopping power regime: a thermal spike description, Nucl. Instrum. Methods Phys. Res. Sect. B 146 (1998) 431–436.
[23] A. Meftah, J.M. Costantini, N. Khalfaoui, S. Boudjadar, J.P. Stoquert, F. Studer, M. Toulemonde, Experimental determination of track cross-section in $Gd_3Ga_5O_{12}$ and comparison to the inelastic thermal spike model applied to several materials, Nucl. Instrum. Methods Phys. Res. B 237 (2005) 563–574.
[24] C. Dufour, A. Audouard, F. Beuneu, J. Dural, J.P. Girard, A. Hairie, M. Levalois, E. Paumier, M. Toulemonde, A high resistivity phase induced by swift heavy ion irradiation of Bi: a probe for thermal spike damage, J. Phys. Condens. Matter 5 (1993) 4573–4584.
[25] C. Dufour, Z.G. Wang, E. Paumier, M. Toulemonde, Transient thermal process induced by swift heavy ions: defect annealing and defect creation in Fe and Ni, Bull. Mater. Sci. 22 (1999) 671–677.
[26] Z.G. Wang, C. Dufour, E. Paumier, M. Toulemonde, The S_e sensitivity of metals under swift-heavy-ion irradiation : a transient thermal process, J. Phys. Condens. Matter 6 (1994) 6733–6750.
[27] C. Dufour, B.L. de Chezelles, V. Delignon, M. Toulemonde, E. Paumier, A transient thermodynamic model for track formation in amorphous semi-conductor: a possible mechanism?, in: P. Mazzoldi (Ed.) Proceedings of Conference on Chemical and Physical Modifications Induced by Irradiation in Glasses, (E-MRS, Strasbourg, volume 61, 1992.
[28] S. Furuno, H. Otsu, K. Hojou, K. Izui, Tracks of high energy heavy ions in solids, Nucl. Instrum. Methods Phys. Res. B 107 (1996) 223–226.
[29] D. Lesueur, A. Dunlop, Damage creation via electronic excitations in metallic targets part II : a theoretical model, Radiat. Eff. Defects Solids 126 (1993) 163–172.
[30] D.K. Avasthi, G.K. Mehta, Swift heavy ions for materials engineering and nanostructuring, Springer Series in Materials Science 145 (2011).
[31] D.K. Avasthi, J.C. Pivin, Ion beam for synthesis and modification of nanostructures, Curr. Sci. 98 (2010) 780–792.
[32] D.K. Avasthi, Modification and characterisation of materials by swift heavy ion, Defence Sci. J. 59 (2009) 401–412.
[33] D.K. Avasthi, Some interesting aspects of swift heavy ions in materials science, Curr. Sci. 78 (2000) 1297–1303.
[34] S. Gupta, F. Singh, N.P. Lalla, B. Das, Swift heavy ion irradiation induced modifications in structural, microstructural ,electrical and magnetic properties of Mn doped SnO_2 thin films, Nucl. Instrum. Methods Phys. Res. B 400 (2017) 37–57.
[35] V.V. Ison, A.R. Rao, V. Dutta, P.K. Kulriya, D.K. Avasthi, S.K. Tripathi, Swift heavy ion induced structural changes in CdS thin films possessing different microstructures: a comparative study, J. Appl. Phys. 106 (2009) 1–7. 023508.
[36] N.G. Deshpande, R. Sharma, Modifications in physical, optical and electrical properties of tin oxide by swift heavy Au^{8+} ion bombardment, Curr. Appl. Phys. 8 (2008) 181–188.
[37] R.S. Chauhan, V. Kumar, D.C. Agarwal, D. Pratap, I. Sulania, A. Tripathi, SHI induced modifications in SnO_2 thin films: structural, optical and surface morphological studies, Nucl. Instrum. Methods Phys. Res. B 286 (2012) 295–298.
[38] K.M. Abhirami, P. Matheswaran, B. Gokul, R. Sathyamoorthy, K. Asokan, Structural and morphological properties of Ag ion irradiated SnO_2 thin films, IOP Conf. Ser. 73 (2015) 1–4. 012113.
[39] F.A. Mir, K.M. Batoo, Effect of Ni and Au ion irradiations on structural and optical properties of nanocrystalline Sb-doped SnO_2 thin films, Appl. Phys. A 122 (2016) 1–7. 418.
[40] T. Mohanty, P.V. Satyam, D. Kanjilal, Synthesis of nanocrystalline tin oxide thin film by swift heavy ion irradiation, J. Nanosci. Nanotechnol. 6 (2006) 2554–2559.
[41] V. Kumar, A. Jain, D. Pratap, D.C. Agarwal, I. Sulania, V.V.S. Kumar, A. Tripathi, S. Varma, R.S. Chauhan, Modifications of nanocrystalline RF sputtered tin oxide thin film using SHI irradiation, Adv. Mater. Lett. 4 (2013) 428–432.
[42] V. Kumar, D. Pratap, A. Jain, D.C. Agarwal, I. Sulania, A. Tripathi, R.J. Chaudhary, R.S. Chauhan, Crystalline to amorphous phase transition of tin oxide nanocrystals induced by SHI at low temperature, AIP Conf. Proc. 715 (2012) 715–716.
[43] A. Sharma, K.D. Verma, M. Varshney, A.P. Singh, Y. Kumar, Growth of nanopillars in SnO_2 thin films by ion irradiation and its gas sensing properties, Adv. Sci. Lett. 4 (2011) 501–507.
[44] H. Thakur, K.K. Sharma, R. Kumar, P. Thakur, A.P. Singh, Y. Kumar, S. Gautam, K.H. Chae, On the optical properties of Ag^{+15} ion beam irradiated TiO_2 and SnO_2 thin films, J. Korean Phys. Soc. 61 (2012) 1609–1614.
[45] K.M. Abhirami, P. Matheswaran, B. Gokul, R. Sathyamoorthy, K. Asokan, Swift heavy ion provoked structural, optical and electrical properties in SnO_2 thin films, Appl. Phys. A 111 (2013a) 1175–1180.
[46] K.M. Abhirami, P. Matheswaran, B. Gokul, R. Sathyamoorthy, D. Kanjilal, K. Asokan, Effect of SHI irradiation on the morphology of SnO_2 thin film prepared by reactive thermal evaporation, Vacuum 90 (2013b) 39–43..
[47] H. Thakur, R. Kumar, P. Thakur, N.B. Brookes, K.K. Sharma, A.P. Singh, Y. Kumar, S. Gautam, K.H. Chae, Orbital anisotropy in SnO_2 thin films and its modification by swift heavy ion irradiation, Chem. Phys. Lett. 511 (2011) 322–325.
[48] S. Rani, N.K. Puri, S.C. Roy, M.C. Bhatnagar, D. Kanjilal, Effect of swift heavy ion irradiation on structure, optical, and gas sensing properties of SnO_2 thin films, Nucl. Instrum. Methods Phys. Res. B 266 (2008a) 1987–1992.
[49] S. Rani, M.C. Bhatnagar, S.C. Roy, N.K. Puri, D. Kanjilal, P-type gas-sensing behaviour of undoped SnO_2 thin films irradiated with a high-energy ion beam, Sens. Actuators B 135 (2008b) 35–39.
[50] R.C. Singh, M.P. Singh, O. Singh, P.S. Chandi, R. Kumar, Effect of 100 Mev O^{7+} ions irradiation on ethanol sensing response of nanostructures of ZnO and SnO_2, Appl. Phys. A 98 (2010) 161–166.
[51] J.F. Ziegler, M.D. Ziegler, J.P. Biersack, Stopping and ranges of ions in matter, SRIM Code (2008). www.srim.org.
[52] J.F. Ziegler, J.P. Biersack, U. Littmark, The Stopping and Range of Ions in Solids, Pergamon, New York, 1985. 1.
[53] M. Batzill, U. Diebold, The surface and materials science of tin oxide, Prog. Surf. Sci. 79 (2005) 47–154.
[54] A. Berthelot, S. Hémon, F. Gourbilleau, C. Dufour, B. Domengés, E. Paumier, Behaviour of a nanometric SnO_2 powder under swift heavy-ion irradiation: from sputtering to splitting, Philos. Mag. A 80 (2000) 2257–2281.
[55] K.N. Yu, Y. Xiong, Y. Liu, C. Xiong, Microstructural change of nano-SnO_2 grain assemblages with the annealing temperature, Phys. Rev. B 55 (1997) 2666–2671.
[56] M.D. McCluskey, M.C. Tarun, S.T. Teklemichael, Hydrogen in oxide semiconductors, J. Mater. Res. 27 (2012) 2190–2198.
[57] A.K. Singh, A. Janotti, M. Scheffler, C.G.V. de Walle, Sources of electrical conductivity in sno_2, Phys. Rev. Lett. 101 (2008) 1–4. 055502
[58] A. Janotti, J.B. Varley, J.L. Lyons, C.G. Van de Walle, et al., Controlling the conductivity in oxide semiconductors, in: J. Wu (Ed.), Functional Metal Oxide Nanostructures, Springer Series in Materials Science, 2012.
[59] A. Janotti, C.G. Van de Walle, Native point defects in ZnO, Phys. Rev. B 76 (2007) 165202–165224.
[60] A. Janotti, C.G. Van de Walle, Fundamentals of zinc oxide as a semiconductor, Rep. Prog. Phys. 72 (2009) 1–29. 126501
[61] A. Janotti, C.G. Van de Walle, Oxygen vacancies in ZnO, Appl. Phys. Lett. 87 (2005) 1–3. 122102
[62] A. Janotti, C.G. Van de Walle, New insights into the role of native point defects in ZnO, J. Cryst. Growth 287 (2006) 58–65.
[63] Ç. Kiliç, A. Zunger, N–type doping of oxides by hydrogen, Appl. Phys. Lett. 81 (2002) 73–75.
[64] W.M. Hlaing Oo, S. Tabatabaei, M.D. McCluskey, J.B. Varley, A. Janotti, C.G. Van de Walle, Hydrogen donors in SnO_2 studied by infrared spectroscopy and first-principles calculations, Phys. Rev. B 82 (01) (2010) 1–4. 1932.
[65] F. Bekisli, M. Stavola, W.B. Fowler, L. Boatner, E. Spahr, G. Lüpke, Hydrogen impurities and shallow donors in SnO_2 studied by infrared spectroscopy, Phys. Rev. B 84 (2011) 1–8. 035213.
[66] J.B. Varley, A. Janotti, A.K. Singh, C.G. Van de Walle, Hydrogen interactions with acceptor impurities in SnO_2: first-principles calculations, Phys. Rev. B 79 (2009) 245206.
[67] P.D.C. King, R.L. Lichti, Y.G. Celebi, J.M. Gil, R.C. Vilão, H.V. Alberto, J.P. Duarte, D.J. Payne, R.G. Egdell, I.M. Kenzie, C.F. McConville, S.F.J. Cox, T.D. Veal, Shallow donor state of hydrogen in In_2O_3 and SnO_2: implications for conductivity in transparent conducting oxides, Phys. Rev. B 80 (2009) 1–4. 081201.
[68] K. Xiong, J. Robertson, S.J. Clark, Behavior of hydrogen in wide band gap oxides, J. Appl. Phys. 102 (2007) 1–13. 083710
[69] C.G. Van de Walle, Hydrogen as a shallow center in semiconductors and oxides, Phys. Status Solidi B 235 (2003) 89–95.
[70] A. Janotti, C.G. Van de Walle, Hydrogen multicentre bonds, Nat. Mater. 6 (2007) 44–47.

[71] S.F.J. Cox, E.A. Davis, S.P. Cottrell, P.J.C. King, J.S. Lord, J.M. Gil, H.V. Alberto, R.C. Vilão, J.P. Duarte, N.A. de Campos, A. Weidinger, R.L. Lichti, S.J.C. Irvine, Experimental confirmation of the predicted shallow donor hydrogen state in zinc oxide, Phys. Rev. Lett. 86 (2001) 2601–2604.
[72] D.G. Thomas, J.J. Lander, Hydrogen as a donor in zinc oxide, J. Chem. Phys. 25 (1956) 1136–1142.
[73] C.G. Van de Walle, Hydrogen as a cause of doping in zinc oxide, Phys. Rev. Lett. 85 (2000) 1012–1015.
[74] G.A. Shi, M. Saboktakin, M. Stavola, S.J. Pearton, Hidden hydrogen in as-grown ZnO, Appl. Phys. Lett. 85 (2004) 5601–5603.
[75] C.G. Van de Walle, J. Neugebauer, Universal alignment of hydrogen levels in semiconductors, insulators and solutions, Nature 423 (2003) 626–628.
[76] N.H. Nickel, Hydrogen migration in single crystal and polycrystalline zinc oxide, Phys. Rev. B 73 (04) (1952) 1–9. 2006
[77] J. Bang, K.J. Chang, Diffusion and thermal stability of hydrogen in ZnO, Appl. Phys. Lett. 92 (2008) 1–3. 132109
[78] J.R. Bellingham, W.A. Phillips, C.J. Adkins, Electrical and optical properties of amorphous indium oxide, J. Phys.: Condens. Matter 2 (1990) 6207–6221.
[79] S. Gupta, B.C. Yadav, P.K. Dwivedi, B. Das, Microstructural, optical and electrical investigations of Sb–SnO_2 thin films deposited by spray pyrolysis, Mater. Res. Bull. 48 (2013) 3315–3322.
[80] R.B.H. Tahar, T. Ban, Y. Ohya, Y. Takahashi, Tin doped indium oxide thin films: electrical properties, J. Appl. Phys. 83 (1998) 2631–2645.
[81] S. Gupta, The Synthesis and Characterization of Transparent Conducting Antimony Doped Tin Oxide Thin Films Deposited by Spray Pyrolysis, M. sc. thesis, Department of Applied Physics, Babasaheb Bhimrao Ambedkar Central University,Lucknow, India, 2012. pp.818
[82] T. Nutz, M. Haase, Wet-chemical synthesis of doped nanomaterials: optical properties of oxygen–deficient and antimony-doped colloidal SnO_2, J. Phys. Chem. B 104 (2000) 8430–8437.
[83] J.W. Orton, M.J. Powell, The hall effect in polycrystalline and powdered semiconductors, Rep. Prog. Phys. 43 (1980) 1263–1307.
[84] V.I. Fistul, V.M. Vainshtein, Mechanism of electron scattering in In_2O_3 films, Sov. Phys. Solid State 8 (1967) 2769.
[85] J.G. Na, Y.R. Cho, Y.H. Kim, T.D. Lee, S.J. Park, Effects of annealing temperature on microstructure and electrical and optical properties of radio-frequency-sputtered tin-doped indium oxide films, J. Am. Ceram. Soc. 72 (1989) 698–701.
[86] V.I. Fistul, Heavily Doped Semiconductors, Plenum Press, New York, 1969. 86.
[87] H.K. Müller, Electrical and optical properties of sputtered In_2O_3 films. I. Electrical properties and intrinsic absorption, Phys. Stat. Sol. 27 (1968a) 723–731.
[88] H.K. Müller, Electrical and optical properties of sputtered In_2O_3 films. II. Optical properties in the near infrared, Phys. Stat. Sol. 27 (1968b) 733–740.
[89] M.C. Flemings, Solidification Processing, London: McGraw–Hill, New York, 1974.